

UNCOVERing the extended strong lensing structures of Abell 2744 with the deepest JWST imaging

Lukas J. Furtak,¹★ Adi Zitrin,¹ John R. Weaver,² Hakim Atek,³ Rachel Bezanson,⁴ Ivo Labbé,⁵ Katherine E. Whitaker,² Joel Leja,^{6,7,8} Sedona H. Price,⁴ Gabriel B. Brammer,⁹ Bingjie Wang (王冰洁),^{6,7,8} Danilo Marchesini,¹⁰ Richard Pan,¹⁰ Pratika Dayal,¹¹ Pieter van Dokkum,¹² Robert Feldmann,¹³ Seiji Fujimoto,^{14,9} Marijn Franx,¹⁵ Gourav Khullar,⁴ Erica J. Nelson¹⁶ and Lamiya A. Mowla¹⁷

¹Physics Department, Ben-Gurion University of the Negev, P.O. Box 653, Be'er-Sheva 84105, Israel

²Department of Astronomy, University of Massachusetts, Amherst, MA 01003, USA

³Institut d'Astrophysique de Paris, CNRS, Sorbonne Université, 98bis Boulevard Arago, 75014, Paris, France

⁴Department of Physics and Astronomy and PITT PACC, University of Pittsburgh, Pittsburgh, PA 15260, USA

⁵Centre for Astrophysics and Supercomputing, Swinburne University of Technology, Melbourne, VIC 3122, Australia

⁶Department of Astronomy & Astrophysics, The Pennsylvania State University, University Park, PA 16802, USA

⁷Institute for Computational & Data Sciences, The Pennsylvania State University, University Park, PA 16802, USA

⁸Institute for Gravitation and the Cosmos, The Pennsylvania State University, University Park, PA 16802, USA

⁹Cosmic Dawn Center (DAWN), Niels Bohr Institute, University of Copenhagen, Jagtvej 128, København N, DK-2200, Denmark

¹⁰Department of Physics and Astronomy, Tufts University, 574 Boston Ave., Medford, MA 02155, USA

¹¹Kapteyn Astronomical Institute, University of Groningen, P.O. Box 800, 9700 AV Groningen, The Netherlands

¹²Department of Astronomy, Yale University, New Haven, CT 06511, USA

¹³Institute for Computational Science, University of Zurich, Winterthurerstrasse 190, CH-8006 Zurich, Switzerland

¹⁴Department of Astronomy, The University of Texas at Austin, Austin, TX 78712, USA

¹⁵Leiden Observatory, Leiden University, P.O. Box 9513, 2100 RA Leiden, Netherlands

¹⁶Department for Astrophysical and Planetary Science, University of Colorado, Boulder, CO 80309, USA

¹⁷Dunlap Institute for Astronomy and Astrophysics, 50 St. George Street, Toronto, Ontario, M5S 3H4, Canada

Accepted 2023 May 25. Received 2023 May 25; in original form 2022 December 16

ABSTRACT

We present a new parametric lens model for the massive galaxy cluster Abell 2744 based on new ultra-deep JWST imaging taken in the framework of the UNCOVER program. These observations constitute the deepest JWST images of a lensing cluster to date, adding to existing deep *Hubble Space Telescope* (HST) images and the recent JWST ERS and DDT data taken for this field. The wide field-of-view of UNCOVER (~ 45 arcmin²) extends beyond the cluster's well-studied central core and reveals a spectacular wealth of prominent lensed features around two massive cluster sub-structures in the north and north-west, where no multiple images were previously known. We identify 75 new multiple images and candidates of 17 sources, 43 of which allow us, for the first time, to constrain the lensing properties and total mass distribution around these extended cluster structures using strong lensing (SL). Our model yields an effective Einstein radius of $\theta_{E,\text{main}} = 23.2'' \pm 2.3''$ for the main cluster core (for $z_s = 2$), enclosing a mass of $M(< \theta_{E,\text{main}}) = (7.7 \pm 1.1) \times 10^{13} M_\odot$, and $\theta_{E,\text{NW}} = 13.1'' \pm 1.3''$ for the newly discovered north-western SL structure enclosing $M(< \theta_{E,\text{NW}}) = (2.2 \pm 0.3) \times 10^{13} M_\odot$. The northern clump is somewhat less massive with $\theta_{E,\text{N}} = 7.4'' \pm 0.7''$ enclosing $M(< \theta_{E,\text{N}}) = (0.8 \pm 0.1) \times 10^{13} M_\odot$. We find the northern sub-structures of Abell 2744 to broadly agree with the findings from weak lensing (WL) analyses and align with the filamentary structure found by these previous studies. Our model in particular reveals a large area of high magnification values between the various cluster structures, which will be paramount for lensed galaxy studies in the UNCOVER field. The model is made publicly available to accompany the first UNCOVER data release.

Key words: gravitational lensing: strong – galaxies: clusters: individual: Abell 2744 – dark matter – galaxies: halos – large-scale structure of the Universe

1 INTRODUCTION

Galaxy clusters are the most massive gravitationally bound structures in the Universe. As such, they form relatively late in the hierarchical cosmic history, around $z \lesssim 1 - 3$ (e.g. [Amoura et al. 2021](#)). Clusters

★ E-mail: furtak@post.bgu.ac.il

form at the nodes of the cosmic web (e.g. [Zeldovich et al. 1982](#); [de Lapparent et al. 1986](#)) where streams of matter and galaxies fall in towards the dense cluster cores, as shown in detailed N-body simulations (e.g. [Klypin & Shandarin 1983](#); [Springel et al. 2005](#); [Dubois et al. 2014](#); [Hatfield et al. 2019](#); [Ata et al. 2022](#)). Indeed, massive galaxy clusters often show merging sub-structures in their central regions, along with disturbed X-ray gas or intra-cluster light (ICL) morphologies, whereas some also show prominent cluster structures far outside their core (e.g. [Borgani & Guzzo 2001](#); [Ebeling et al. 2004](#); [Kartaltepe et al. 2008](#); [Jauzac et al. 2012, 2016, 2018](#); [Medezinski et al. 2016](#); [Durret et al. 2016](#); [Ellien et al. 2019](#); [Kim et al. 2019](#); [Asencio et al. 2021](#); [Diego et al. 2023](#)). The existence, and the observed number of the most massive galaxy clusters can be confronted with expectations from Λ CDM cosmology (e.g. [Mullis et al. 2005](#); [Ebeling et al. 2007](#); [Foley et al. 2011](#); [Stanford et al. 2012](#); [Wang et al. 2016](#); [Miller et al. 2018](#); [Asencio et al. 2021](#)) and therefore help constrain the formation and evolution of large-scale structures in the Universe.

One of the most direct methods to detect massive clusters and constrain their total matter distributions is through their gravitational lensing signatures. Although the triaxial shape of clusters creates some bias towards clusters that are elongated along the light of sight (e.g. [Hennawi et al. 2007](#); [Serenio et al. 2010](#); [Okabe et al. 2010](#); [Oguri et al. 2012](#)), strong lensing (SL) clusters showing a large number of multiply imaged features are often also the most massive galaxy clusters. These are usually either more concentrated, with higher masses in their central core (e.g. [Broadhurst et al. 2008](#); [Broadhurst & Barkana 2008](#)), or yet un-virialized merging systems with multiple cores and dark matter (DM) sub-structures enhancing the SL regime (e.g. [Meneghetti et al. 2003, 2007a,b](#); [Torri et al. 2004](#); [Redlich et al. 2012](#); [Zitrin et al. 2013a](#)). Gravitational lensing, and in particular the SL regime, thus represents a unique means to probe the otherwise invisible DM distribution in massive galaxy clusters.

Galaxy clusters also act as ‘cosmic telescopes’: The gravitational magnification of background objects allows us to detect and study high-redshift galaxies that would otherwise be too faint to be observed (e.g. [Maizy et al. 2010](#); [Kneib & Natarajan 2011](#); [Sharon et al. 2012](#); [Zitrin et al. 2014](#); [Monna et al. 2014](#); [Richard et al. 2014](#); [Coe et al. 2015, 2019](#)). Indeed, several observational campaigns targeting galaxy clusters undertaken over the past decade with the *Hubble Space Telescope* (HST), often complemented by ground-based observations, have led to the detection of several hundreds of lensed high-redshift galaxies at $z > 6$, down to UV luminosities of $M_{UV} \lesssim -13$ (e.g. [Livermore et al. 2017](#); [Bouwens et al. 2017, 2022](#); [Ishigaki et al. 2018](#); [Atek et al. 2018](#)) and stellar masses $M_{\star} \gtrsim 10^6 M_{\odot}$ ([Bhatawdekar et al. 2019](#); [Kikuchihara et al. 2020](#); [Furtak et al. 2021](#); [Strait et al. 2020, 2021](#)). These campaigns to observe SL clusters have also enabled the spectacular detections of transient phenomena such as lensed supernovae (e.g. [Kelly et al. 2015, 2016a,b](#); [Rodney et al. 2015, 2021](#)) and even single stars (e.g. [Kelly et al. 2018](#); [Welch et al. 2022](#); [Meena et al. 2023a](#)).

Abell 2744 (e.g. [Abell et al. 1989](#); [Allen 1998](#); [Ebeling et al. 2010](#)) at $z_d = 0.308$ has by now become a well-studied galaxy cluster. Largely owing to its lensing strength, it was chosen for the *Hubble Frontier Fields* (HFF; [Lotz et al. 2017](#)) program, an HST Director’s Discretionary Time (DDT) program that targeted six lensing clusters to unprecedented depth. Abell 2744 has also been extensively targeted by other ground- and space-based follow-up programs. In terms of SL analyses, the main cluster core was first analyzed in [Merten et al. \(2011\)](#) using the Light-Traces-Mass modeling method (LTM; [Zitrin et al. 2009](#)), revealing a large number of multiply imaged systems. [Merten et al. \(2011\)](#) also used X-ray data and performed a

wider-field weak lensing (WL) analysis, finding other massive structures around the main clump, which already hinted at the merging history of the cluster. Several lens modeling teams have since published SL models for the core of Abell 2744 based on HFF imaging and spectroscopic follow-up campaigns ([Richard et al. 2014](#); [Johnson et al. 2014](#); [Wang et al. 2015](#); [Jauzac et al. 2015](#); [Kawamata et al. 2016, 2018](#); [Prieue et al. 2017](#)). These also yielded numerous lensed high-redshift galaxies behind Abell 2744 (e.g. [Zheng et al. 2014](#); [Atek et al. 2014, 2015](#); [Ishigaki et al. 2015](#)), including a triply imaged $z \sim 10$ galaxy ([Zitrin et al. 2014](#)), recently confirmed spectroscopically by [Roberts-Borsani et al. \(2022\)](#), and a multiply imaged candidate system at $z \sim 7 - 8$ ([Atek et al. 2014](#); [Mahler et al. 2018](#)), which we confirm is a triply-imaged high-redshift object. This particular object seems to be a uniquely red and compact high-redshift object, potentially quasar-like, as presented in detail in a dedicated paper [Furtak et al. \(2022\)](#). The detailed WL studies in a wide field around the core revealed substantial extended DM sub-structures to the far north and north-west of the cluster core, which seem to hint at a large-scale filamentary structure ([Medezinski et al. 2016](#); [Jauzac et al. 2016](#)). The most recent SL models of the cluster were published by [Mahler et al. \(2018\)](#), refined in [Richard et al. \(2021\)](#), and by [Bergamini et al. \(2022\)](#). The [Mahler et al. \(2018\)](#) model is constrained by 188 multiple images, many of which are photometric, and the [Bergamini et al. \(2022\)](#) model includes 90 spectroscopically confirmed multiple images in the main cluster center. Both of these state-of-the-art models included DM halo components far ($\sim 3'$) outside the main cluster core. These were included to account for the substructures discovered in previous WL analyses, and following galaxy over-densities seen in wider-field HST imaging around the cluster. However, due to the lack of ultra-deep high-resolution imaging, and thus SL constraints far from the cluster center, these external DM halos were not directly constrained in these models¹.

This now changes thanks to the unprecedented sensitivity and spatial resolution of the JWST ([Gardner et al. 2006](#); [McElwain et al. 2023](#)), the advent of which has already revealed numerous new SL features in several clusters and enabled significant improvements to their SL models ([Mahler et al. 2023](#); [Pascale et al. 2022](#); [Caminha et al. 2022](#); [Diego et al. 2023](#); [Hsiao et al. 2022](#); [Williams et al. 2023](#); [Meena et al. 2023b](#)). Most recently, the JWST targeted Abell 2744 in the framework of the *Ultra-deep NIRSpec and NIRCам Observations before the Epoch of Reionization* (UNCOVER) program (PIs: I. Labbé & R. Bezanson; [Bezanson et al. 2022](#)) for wide-field ultra-deep imaging of the cluster and its surroundings (it was also observed to lesser depth in two other JWST programs; see section 2). These new observations now reveal spectacular multiple imaging and strongly lensed arcs also outside the core of Abell 2744, namely around the northern and most prominently the north-western sub-structures. In this work, we use the UNCOVER imaging to identify and classify these new SL constraints and for the first time directly constrain the northern and north-western extensions of the cluster, with a total of 43 new multiple images. These are then incorporated into a new parametric SL model containing the entire central UNCOVER field-of-view, covering a total area of about $7.6' \times 7.6'$. The lensing maps of our model are made publicly available as part of the UNCOVER data product release².

This paper is organized as follows: We briefly present the targeted

¹ Though see our latest HST-based model used in [Roberts-Borsani et al. \(2022\)](#) where we included three tentative multiple systems identified around the two northern clumps in archival HST data in a first attempt to constrain these sub-structures.

² The maps can be found in the following repository: <https://>

cluster and the data used in this analysis in section 2, before describing our modeling methods and the newly identified lensed features used to constrain our SL model in section 3. We present and discuss the results in section 4 and the work is concluded in section 5. Throughout this paper, we assume a standard flat Λ CDM cosmology with $H_0 = 70 \frac{\text{km}}{\text{sMpc}}$, $\Omega_\Lambda = 0.7$, and $\Omega_m = 0.3$. All magnitudes quoted are in the AB system (Oke & Gunn 1983) and all quoted uncertainties represent 1σ ranges unless stated otherwise.

2 OBSERVATIONS AND DATA

As one of the six HFF clusters, Abell 2744 (A2744 hereafter) is a well-studied gravitational lensing system and has been targeted by many imaging and spectroscopic campaigns spanning multiple wavelength regimes. Among the ancillary data, the most relevant for our current study are of course the HFF HST images, which were recently complemented with the *Beyond Ultra-deep Frontier Fields And Legacy Observations* (BUFFALO; PIs: C. Steinhardt & M. Jauzac; Steinhardt et al. 2020) to extend the area of the HST coverage around the cluster center. In addition, there were extensive spectroscopic campaigns of the HFF clusters, both with the HST from space in e.g. the *Grism Lens-Amplified Survey from Space* survey (GLASS; Treu et al. 2015) and from the ground with *Keck* and ESO's *Very Large Telescope* (VLT). The former was recently complemented with the first JWST spectroscopy of A2744 in the framework of the GLASS-JWST Early Release Science (ERS) program (Treu et al. 2022) targeted at the cluster core. A2744 is also part of the *ALMA Frontier Fields* survey (González-López et al. 2017) which obtained 1.1 mm imaging of the cluster core with the *Atacama Large Millimeter/sub-millimeter Array* (ALMA) Band 6 and which will be complemented with additional observations covering the entire UNCOVER footprint (Program ID: 2022.1.00073.S; PI: S. Fujimoto).

In the following, we concentrate on the data sets that are directly used in this study to construct our SL model of the cluster, i.e. the UNCOVER JWST imaging in section 2.1 and existing HST imaging and ground-based spectroscopy in section 2.2.

2.1 JWST UNCOVER imaging

The UNCOVER imaging of A2744 comprises extremely deep observations of the cluster and its surrounding field with the *Near Infrared Camera* (NIRCam; Rieke et al. 2005, 2023) aboard the JWST, achieving nominal 5σ depths of the order of 29.8 magnitudes before accounting for magnification. The magnification on average adds ~ 2 magnitudes to the depths in the SL regime, so that UNCOVER effectively reaches down to ~ 32 magnitude. The cluster was observed in six broad-band filters, F115W, F150W, F200W, F277W, F356W and F444W, and in one medium-band filter, F410M, for 4-6 hours each. The data were then reduced and drizzled into mosaics with the *grism redshift and line analysis software for space-based spectroscopy* (grizli³; Brammer et al. in prep.). These mosaics also incorporate the other public JWST imaging data available in the vicinity of A2744, namely the GLASS-JWST (Treu et al. 2022) images obtained with NIRCam and the *Near-Infrared Imager and Slitless Spectrograph* (NIRISS; Doyon et al. 2012, Doyon

et al. in prep.), which in particular add F090W-band coverage in parts of the UNCOVER field, and the NIRCam imaging obtained in DDT program 2767 (PI: P. Kelly). For this work we use the v5.4 UNCOVER mosaics, which are publicly available on the UNCOVER website⁴ and will also soon be available on the Barbara A. Mikulski Archive for Space Telescopes (MAST). We refer the reader to the UNCOVER survey paper (Bezanson et al. 2022) for more details on the JWST data. With a field-of-view totaling $\sim 45 \text{ arcmin}^2$, the UNCOVER mosaics represent the widest ultra-deep imaging coverage of A2744 to date. Note that deep *Near Infrared Spectrograph* (NIRSpec; Jakobsen et al. 2022; Ferruit et al. 2022; Böker et al. 2023) observations for UNCOVER are scheduled for July 2023.

In our analysis we furthermore use the first team-internal versions of the UNCOVER photometric catalogs, produced with a python implementation of SExtractor (SEP; Bertin & Arnouts 1996; Barbary 2016; Barbary 2018), which will be published in subsequent UNCOVER data releases as detailed in Weaver et al. (2023). These catalogs also contain photometric redshifts measured with EAZY (Brammer et al. 2008) and gravitational magnifications derived from the lens model presented in this work.

2.2 Archival HST and ground-based data

In addition, the UNCOVER data products encompass HST mosaics drizzled to the same pixel-scale and WCS grid as the JWST imaging with grizli. Therefore, we also incorporate the HFF and extended-area BUFFALO observations in the *Advanced Camera for Surveys* (ACS) F435W, F606W and F814W filters, and the *Wide-Field Camera Three* (WCF3) F105W, F125W, F140W and F160W filters in our analysis.

We make use of the spectroscopic redshift catalogs constructed by Mahler et al. (2018), refined in Richard et al. (2021), and Bergamini et al. (2022). These were measured using the deep and wide-field observations of A2744 obtained with the *Multi-Unit Spectroscopic Explorer* (MUSE; Bacon et al. 2010) on the VLT in the framework of the MUSE guaranteed time observations (GTO; Program ID: 094.A-0115; PI: J. Richard). The data reduction is described in detail in Richard et al. (2021). Additional redshifts for cluster galaxies used in this work were compiled in Bergamini et al. (2022) using data from GLASS, *Visible Multi-Object Spectrograph* (VIMOS; Braglia et al. 2009), and *Anglo-Australian Telescope* (AAT; Owers et al. 2011).

3 STRONG LENSING MASS MODELING

In this section, we present our methods and the constraints used to construct the mass model of A2744. The lens modeling code is explained in section 3.1. Our SL mass model of A2744 essentially takes two input components from the imaging and spectroscopy data: the cluster member galaxies (section 3.2) and the lensed multiple image systems (section 3.3). Finally, we explain our initial setup of the A2744 SL model in section 3.4.

3.1 Modeling method

To model A2744 we use a code recently developed for fast parametric lens modeling of galaxy clusters. The method is an updated version of the previous (grid-based) parametric method presented in

[jwst-uncover.github.io/DR1.html#LensingMaps](https://github.com/jwst-uncover/DR1.html#LensingMaps), which is part of the UNCOVER website <https://jwst-uncover.github.io>.

³ <https://github.com/gbrammer/grizli>

⁴ <https://jwst-uncover.github.io/DR1.html>

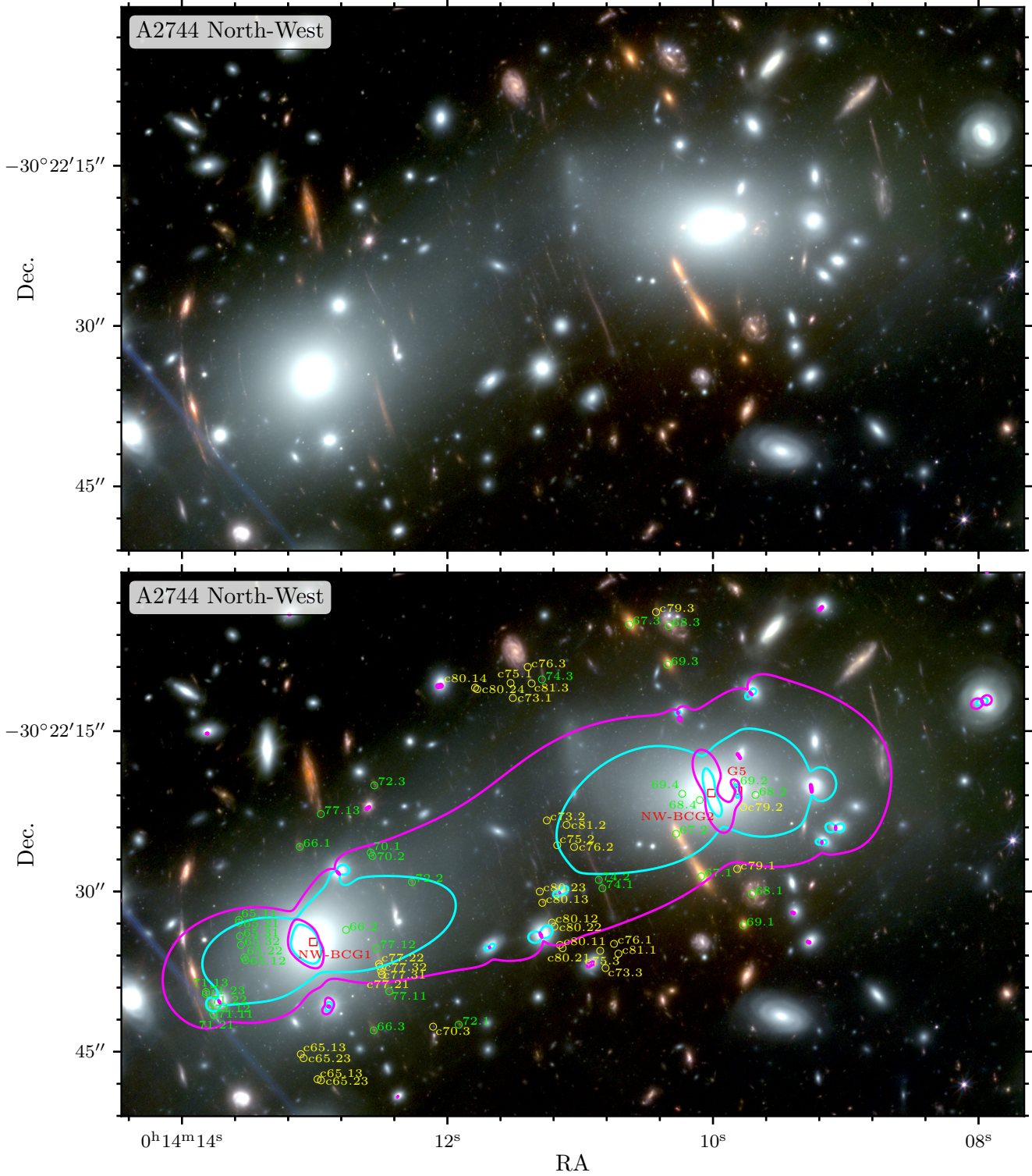


Figure 1. A $1.46' \times 0.85'$ cutout of an UNCOVER color-composite image exhibiting the many newly discovered SL features and candidates in the north-western sub-structure of A2744. The filter stacks used are: Blue – F090W+F115W+F150W, Green – F200W+F277W and Red – F356W+F410M+F444W. In the bottom panel, we mark the newly identified and numbered multiple image systems in green and multiple image candidates in yellow. These are listed in Tab. 1. Cluster galaxies left free to vary in our SL model (see Tab. 3) are shown in red. The critical curves of our SL model (see section 4) for source redshifts $z_s = 1.6881$, the redshift of system 1 (Mahler et al. 2018), and $z_s = 10$ are shown in blue and purple, respectively.

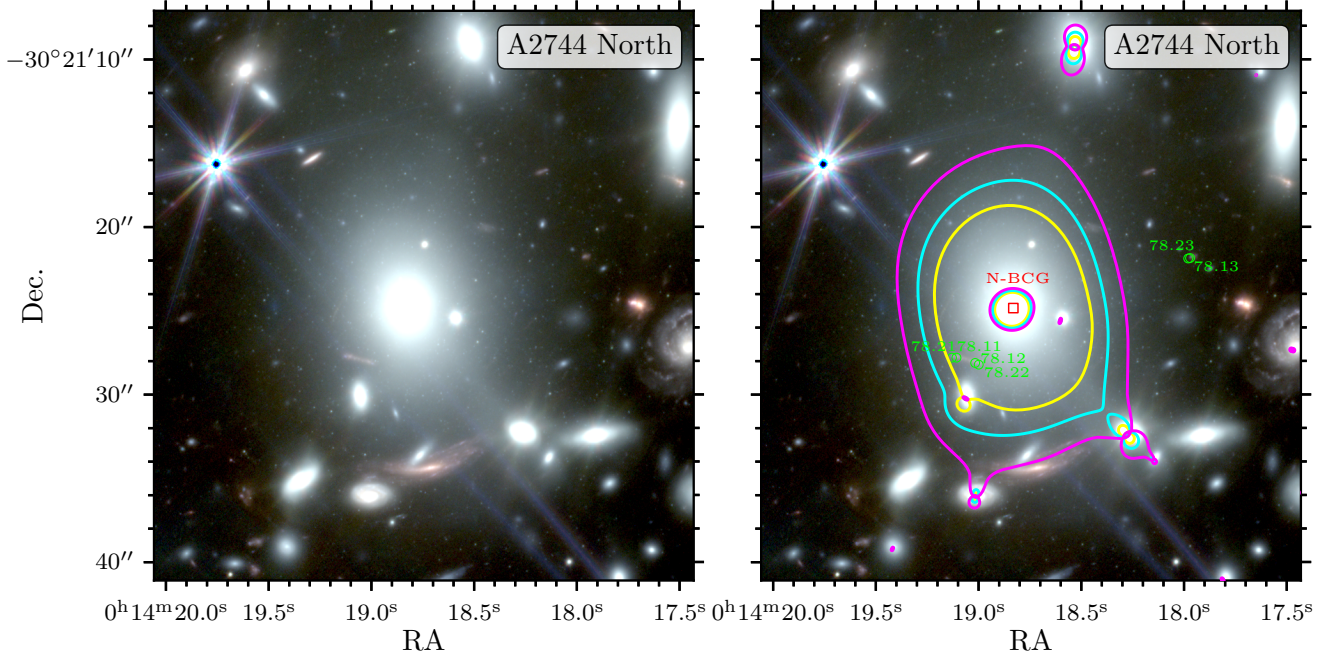


Figure 2. A $34'' \times 34''$ cutout of an UNCOVER color-composite image in the same filter configuration as in Fig. 1. In the right-hand panel, we mark the newly identified SL features around the northern sub-structure of A2744. The northern BCG, which is left free to vary in our SL model, is shown in red. We also show the critical curves of our SL model (see section 4) for source redshifts $z_s = 1$ in yellow, $z_s = 1.6881$ (see Fig. 1) in blue and $z_s = 10$ in purple. The critical curves from the current model do not pass where we would expect for system 78, suggesting that the system either lies at a lower redshift ($z_s < 1$), that it consists only of two images, or most probably, that the mass of this sub-halo is somewhat overestimated (see discussion in section 4). A red spiral galaxy south of the N-BCG is notably lensed, i.e. magnified and distorted, but is likely not multiply imaged.

Zitrin et al. (2013a,b, 2015); Zitrin (2021), revised to now be completely “analytic” in the sense that the model is not limited by an input grid resolution. The code was tested on self-simulated mock mass distributions: Using the same mass parametrizations as used for the modeling, a suite of order ~ 10 arbitrary mass distributions was generated by specifying for each one the input parameter values (namely core and truncation radii, and velocity dispersion of a reference galaxy, and the various DM halo parameters). We then planted sources behind the cluster and lensed them through the simulated mock cluster lens to predict the locations of their multiple images. SL models for these mock clusters were then constructed using these multiple images as input for the minimization, in order to test how well the input parameter values can be recovered. The code was found to work very well, recovering the input parameters to well below the 1σ errors, both using lens and source plane minimizations. First successful models using this method with JWST data were published in Pascale et al. (2022) for SMACS J0723.3-7327, where initial details about the modeling method were given, in Hsiao et al. (2022) and Meena et al. (2023b) for MACS J0647.7+7015, and in Williams et al. (2023) for RX J2129.4+0009. An HST-based A2744 model with this method was recently also used in Roberts-Borsani et al. (2022). The code is sometimes referred to as “Zitrin-Analytic” in these works.

The method is similar in essence to other, commonly used parametric techniques (e.g. lenstool (Kneib et al. 1996; Jullo et al. 2007; Jullo & Kneib 2009), glafic (Oguri et al. 2010), GLEE (Halkola et al. 2006; Grillo et al. 2015), etc.), and consists of two main mass components. The first mass component comprises the cluster galax-

ies, each galaxy modeled as a double Pseudo Isothermal Ellipsoid (dPIE; Elíasdóttir et al. 2007) with projected surface mass density:

$$\Sigma(\xi) = \frac{\sigma_v^2 r_{\text{cut}}^2}{2G(r_{\text{cut}}^2 + r_{\text{core}}^2)} \left[\left(1 + \frac{r_{\text{core}}^2}{\xi^2} \right)^{-\frac{1}{2}} - \left(1 + \frac{r_{\text{cut}}^2}{\xi^2} \right)^{-\frac{1}{2}} \right], \quad (1)$$

where σ_v , r_{core} and r_{cut} are the velocity dispersion, core radius, and truncation radius, respectively, and ξ is an elliptical coordinate defined as:

$$\xi^2 = \frac{x^2}{(1-\epsilon)^2} + \frac{y^2}{(1+\epsilon)^2}, \quad (2)$$

with ellipticity ϵ . In order to optimize the computation speed, we model most cluster galaxies as spherical ($\epsilon = 0$). The ellipticity is used however for brightest cluster galaxies (BCGs) and eq. 1 is in practice implemented as in e.g. Keeton (2001) and Oguri et al. (2010), where it is referred to as a “Pseudo-Jaffe profile” after Jaffe (1983). The total mass associated with a dPIE profile is then

$$M_{\text{tot}} = \frac{\pi \sigma_v^2}{G} \frac{r_{\text{cut}}^2}{r_{\text{cut}} + r_{\text{core}}}. \quad (3)$$

In order to drastically reduce the otherwise large number of free parameters that would arise from modeling each cluster galaxy individually, we use common scaling relations:

$$\sigma_v = \sigma_{v,\star} \left(\frac{L}{L_\star} \right)^\lambda, \quad (4)$$

$$r_{\text{core}} = r_{\text{core},\star} \left(\frac{L}{L_\star} \right)^\beta, \quad (5)$$

$$r_{\text{cut}} = r_{\text{cut},\star} \left(\frac{L}{L_\star} \right)^\alpha, \quad (6)$$

which are based on e.g. the the Tully-Fisher (Tully & Fisher 1977) and Faber-Jackson relations (Faber & Jackson 1976) and the fundamental plane to tie the individual dPIE parameters of each galaxy to its luminosity L and scale them with respect to a reference galaxy (e.g. Halkola et al. 2006, 2007; Jullo et al. 2007; Monna et al. 2014, 2015). The three parameters $\sigma_{v,\star}$, $r_{\text{core},\star}$ and $r_{\text{cut},\star}$ are those of a reference galaxy of luminosity L_\star and can be left as free parameters in the model. Note that $r_{\text{core},\star}$ is typically fixed however and only σ_\star and $r_{\text{cut},\star}$ are iterated for. The scaling parameters λ , β and α can also be left as free parameters in the modeling. For example, Jullo et al. (2007) use $\lambda = 0.25$, $\beta = 0.5$ and $\alpha = 0.5$, for a constant mass-to-light ratio, or $\alpha = 0.8$ to more closely match the fundamental plane. As another example, Monna et al. (2015) for instance, do not adopt a core for the galaxies, and have $\lambda = 0.3$ and $\alpha = 0.4$. Note that unless these are specifically left to vary freely, the scaling relations (4)–(6) are also applied to the BCGs.

The second mass component consists of the diffuse cluster dark matter halos. These are modeled as Pseudo Isothermal Elliptical Mass Distributions (PIEMDs; e.g. Jaffe 1983; Keeton 2001)

$$\Sigma(\xi) = \frac{\sigma_v^2}{2G} \left(r_{\text{core}}^2 + \xi^2 \right)^{-\frac{1}{2}}. \quad (7)$$

One such diffuse cluster halo is usually sufficient for a relaxed cluster with a single prominent BCG, but several cluster halos are often needed to model merging or complex clusters, i.e. those containing various sub-structures and BCGs such as A2744 (e.g. Jauzac et al. 2015; Mahler et al. 2018; Bergamini et al. 2022).

In addition, a two-component external shear can be applied, which can sometimes help account for external contributions not taken into account in the mass modeling. Source redshifts can be left as free parameters, especially for galaxies lacking spectroscopic redshifts, and the weight of individual cluster galaxies can also be left to be freely optimized. The latter can be applied in two ways – either by incorporating the relative weight factor directly to the luminosity of the galaxy, affecting correspondingly all quantities derived from the scaling relations (this is the default choice), or if desired, only to the velocity dispersion of the galaxy, without affecting its other parameters. Similarly, the ellipticity parameters and core radii of the BCGs can also be left to be freely optimized. Finally, the code also allows for the incorporation of time delays, magnification ratios, and image parity information.

3.2 Cluster member galaxies

We compile the list of cluster member galaxies hierarchically using all of the available data sets in the following way: We first include the 225 cluster members used in Bergamini et al. (2022), 202 of which are spectroscopically confirmed to lie at the cluster redshift, $z_d = 0.308$. These were mostly derived from MUSE observations, as well as other ancillary catalogs listed in section 2.2. This spectroscopic sample is then used to calibrate red-sequence selection criteria aimed at identifying cluster member galaxies that lie beyond the MUSE coverage.

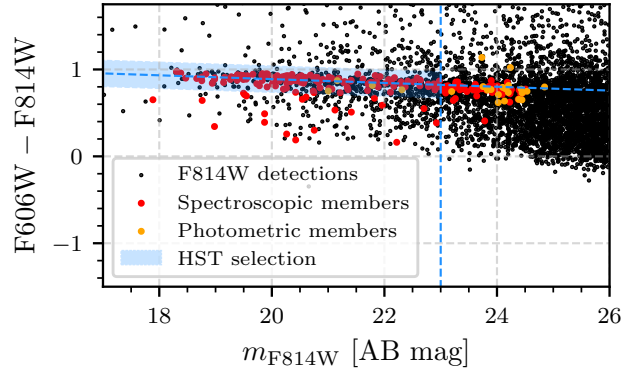


Figure 3. HST color-magnitude diagram of objects detected in A2744, showing the cluster’s red sequence. The known cluster members from Bergamini et al. (2022) are shown in red and orange dots and our red sequence selection is shown as the blue shaded area.

At the cluster redshift, the 4000 Å-break falls between the HST/ACS F606W and F814W bands. Because of that, these two filters are optimal for identifying the red sequence of A2744. We therefore perform a cluster member selection using the HST data (see section 2.2) which are much more extended than the initial HFF footprint owing to the wide-field BUFFALO and parallel field data. Galaxies are detected with SExtractor (Bertin & Arnouts 1996) in the F814W-band and photometry is measured in both ACS bands. The thus obtained color-magnitude diagram clearly shows the cluster’s red sequence, as can be seen in Fig. 3. We fit a linear relation to the F606W-F814W color of the Bergamini et al. (2022) spectroscopic cluster members and use the result to select HST-detected galaxies in a color window of width 0.3 magnitudes around that relation with magnitudes $m_{F814W} \leq 23$ mag as cluster members. Note that this magnitude cut is only applied to the color-selected galaxies, we include all spectroscopically confirmed cluster members regardless of their brightness.

With this selection, we end up with a cluster member catalog containing 421 galaxies. Most notable are of course the two well-known brightest cluster galaxies (BCGs), BCG1 and BCG2, in the cluster core. In addition, the cluster has two BCGs at the position of the north-western extension, which we will denote NW-BCG1 and NW-BCG2, and one in the northern sub-structure which we will denote N-BCG. While these sub-structures were included as fixed or free DM clumps in previous SL models of A2744 (Mahler et al. 2018; Bergamini et al. 2022), we are able to confirm them as SL structures for the first time thanks to the UNCOVER imaging and constrain their parameters as will be shown in more detail in sections 3.3 and 4. The wide HST coverage of the UNCOVER field reveals cluster member galaxies out to 4.11’ from BCG1, which corresponds to 1.12 Mpc at the cluster redshift. Together with the JWST UNCOVER data revealing a trove of SL constraints (see section 3.3), these now confirm the extended merging nature of A2744 already indicated by the previous X-ray and WL analyses (Merten et al. 2011; Medezinski et al. 2016; Jauzac et al. 2016). Note that we will further discuss the large-scale structure of A2744 in light of our SL analysis results in section 4. The full catalog of cluster galaxies is included in the public release of our SL model of A2744 (see section 4).

Table 1. New multiple images and candidates identified in the northern and north-western extensions of A2744.

ID	RA	Dec.	z_{phot} [97.5 %-range]	z_{model} [95 %-range]	Remarks
65.11	00:14:13.570	-30:22:32.649	-	2.798 [2.473, 3.106]	Close to north-western BCG1.
65.12	00:14:13.521	-30:22:36.422	-	"	"
c65.13	00:14:13.105	-30:22:45.219	3.483 [3.258, 3.741]	"	Candidate counter image.
c65.13	00:14:12.979	-30:22:47.563	-	"	"
65.21	00:14:13.571	-30:22:32.916	-	"	Close to north-western BCG1.
65.22	00:14:13.530	-30:22:36.165	-	"	"
c65.23	00:14:13.084	-30:22:45.594	-	"	Candidate counter image.
c65.23	00:14:12.953	-30:22:47.671	-	"	"
65.31	00:14:13.563	-30:22:34.178	-	"	Close to north-western BCG1.
65.32	00:14:13.556	-30:22:35.004	-	"	"
66.1	00:14:13.113	-30:22:25.817	2.227 [1.994, 2.421]	2.413 [2.406, 2.420]	
66.2	00:14:12.764	-30:22:33.592	-	"	Close to north-western BCG1.
66.3	00:14:12.556	-30:22:43.000	-	"	
67.1	00:14:10.089	-30:22:28.583	2.423 [2.288, 2.510]	2.617 [2.613, 2.620]	Bright system, invisible in HST data,
67.2	00:14:10.279	-30:22:24.600	2.536 [2.491, 2.695]	"	
67.3	00:14:10.632	-30:22:05.019	2.443 [2.347, 2.600]	"	
68.1	00:14:09.707	-30:22:30.242	2.524 [2.495, 2.698]	2.327 [2.321, 2.332]	Bright system, invisible in HST data.
68.2	00:14:09.681	-30:22:20.969	-	"	Close to north-western BCG2.
68.3	00:14:10.334	-30:22:05.143	2.443 [2.234, 2.621]	"	
68.4	00:14:10.100	-30:22:21.444	-	"	Radial image; close to north-western BCG2.
69.1	00:14:09.773	-30:22:33.161	2.423 [2.228, 2.630]	2.432 [2.428, 2.436]	Bright system, invisible in HST data.
69.2	00:14:09.823	-30:22:19.990	-	"	Close to north-western BCG2.
69.3	00:14:10.344	-30:22:08.778	2.325 [2.224, 2.351]	"	
69.4	00:14:10.233	-30:22:20.856	-	"	Radial image; close to north-western BCG2.
70.1	00:14:12.579	-30:22:26.363	-	2.716 [2.500, 3.645]	
70.2	00:14:12.565	-30:22:26.675	-	"	
c70.3	00:14:12.109	-30:22:42.648	-	"	
71.11	00:14:13.764	-30:22:41.450	-	1.379 [1.245, 1.533]	
71.12	00:14:13.788	-30:22:40.884	-	"	
71.13	00:14:13.819	-30:22:39.388	-	"	
71.21	00:14:13.759	-30:22:41.574	-	"	
71.22	00:14:13.797	-30:22:40.744	-	"	
71.23	00:14:13.819	-30:22:39.597	-	"	
72.1	00:14:11.915	-30:22:42.461	3.657 [3.131, 4.088]	3.544 [3.531, 3.565]	
72.2	00:14:12.268	-30:22:29.121	-	"	
72.3	00:14:12.552	-30:22:20.067	3.664 [3.234, 4.086]	"	
c73.1	00:14:11.508	-30:22:11.886	0.225 [0.042, 6.799]	-	
c73.2	00:14:11.252	-30:22:23.351	4.037 [1.173, 5.340]	-	
c73.3	00:14:10.810	-30:22:37.163	-	-	
74.1	00:14:10.833	-30:22:29.697	2.707 [1.324, 4.563]	3.033 [2.832, 3.255]	
74.2	00:14:10.861	-30:22:28.911	4.451 [1.913, 4.921]	"	
74.3	00:14:11.289	-30:22:10.152	2.228 [1.834, 2.523]	"	
c75.1	00:14:11.525	-30:22:10.488	2.040 [0.409, 11.036]	-	
c75.2	00:14:11.174	-30:22:25.668	5.062 [1.103, 16.824]	-	
c75.3	00:14:10.850	-30:22:35.548	-	-	
c76.1	00:14:10.746	-30:22:34.898	-	-	
c76.2	00:14:11.046	-30:22:25.827	0.798 [0.113, 1.915]	-	
c76.3	00:14:11.396	-30:22:08.988	-	-	

Note. – *Column 1:* Image ID. – *Columns 2 and 3:* Right ascension and declination (J2000.0). – *Column 4:* Photometric redshift and its 97.5 % range taken from the UNCOVER catalog (see section 2.1). – *Column 5:* Median redshift from our SL-model (see section 4). – *Column 6:* Additional remarks. Candidate images are marked with “c” and are not used in the modeling.

Table 1 – *continued* New multiple images and candidates identified in the northern and north-western extensions of A2744. We also include here two systems lensed by the main cluster core: the $z \approx 9.8$ system from (Zitrin et al. 2014; Roberts-Borsani et al. 2022), and one dropout $z \sim 7 - 8$ system (i.e. system 53 Atek et al. 2014; Mahler et al. 2018), that we further confirm with the UNCOVER data. Note that system 53 is not included in the lens modeling at this stage.

ID	RA	Dec.	z_{phot} [97.5 %-range]	z_{model} [95 %-range]	Remarks
77.11	00:14:12.439	-30:22:39.334	-	1.505 [1.441, 1.582]	
77.12	00:14:12.535	-30:22:35.316	-	"	
77.13	00:14:12.954	-30:22:22.743	-	"	
c77.21	00:14:12.493	-30:22:37.781	-	"	
c77.22	00:14:12.516	-30:22:36.783	-	"	
c77.31	00:14:12.501	-30:22:37.430	-	"	
c77.32	00:14:12.511	-30:22:37.016	-	"	
78.11	00:14:19.108	-30:21:27.791	-	2.571 [2.049, 2.767]	Close to northern BCG.
78.12	00:14:19.017	-30:21:28.108	-	"	"
78.13	00:14:17.971	-30:21:21.851	-	"	
78.21	00:14:19.130	-30:21:27.791	-	"	Close to northern BCG.
78.22	00:14:19.000	-30:21:28.209	-	"	System redshift poorly constrained.
78.23	00:14:17.980	-30:21:21.877	-	"	
c79.1	00:14:09.818	-30:22:27.889	2.606 [2.223, 2.963]	-	
c79.2	00:14:09.772	-30:22:22.089	-	-	Close to north-western BCG2.
c79.3	00:14:10.429	-30:22:03.847	-	-	
c80.11	00:14:11.153	-30:22:35.005	-	-	Candidate high-redshift object; possible F814W-dropout.
c80.12	00:14:11.213	-30:22:32.917	-	-	"
c80.13	00:14:11.286	-30:22:31.056	-	-	"
c80.14	00:14:11.793	-30:22:10.935	0.706 [0.541, 13.853]	-	"
c80.21	00:14:11.133	-30:22:35.298	11.839 [0.993, 15.925]	-	"
c80.22	00:14:11.195	-30:22:33.287	-	-	"
c80.23	00:14:11.305	-30:22:30.000	15.104 [1.056, 19.585]	-	"
c80.24	00:14:11.776	-30:22:11.062	12.357 [0.537, 14.560]	-	"
c81.1	00:14:10.713	-30:22:35.817	-	-	
c81.2	00:14:11.104	-30:22:23.761	-	-	
c81.3	00:14:11.367	-30:22:10.528	-	-	
53.1	00:14:19.161	-30:24:05.664	7.188 [7.142, 7.165]	-	Detected in HFF (Atek et al. 2014; Mahler et al. 2018).
53.2	00:14:20.051	-30:23:48.058	0.193 [0.189, 0.196]	-	"; heavily affected by the ICL.
53.3	00:14:23.331	-30:23:39.639	7.188 [7.131, 8.578]	-	Newly identified in the UNCOVER imaging (Furtak et al. 2022).
JD1A	00:14:22.202	-30:24:05.364	$z_{\text{spec}} = 9.76$	-	see Zitrin et al. (2014); Roberts-Borsani et al. (2022)
JD1B	00:14:22.805	-30:24:02.700	"	-	"
cJD1C	00:14:18.607	-30:24:31.356	"	-	"

Note. – *Column 1:* Image ID. – *Columns 2 and 3:* Right ascension and declination (J2000.0). – *Column 4:* Photometric redshift and its 97.5 % range taken from the UNCOVER catalog (see section 2.1). – *Column 5:* Median redshift from our SL-model (see section 4). – *Column 6:* Additional remarks. Candidate images are marked with “c” and are not used in the modeling.

3.3 Multiple image systems

The SL features at the center of A2744 have been extensively studied with the exceptionally deep HFF imaging and GLASS and MUSE spectroscopy (see section 2.2). These data yielded a total of 60 multiply imaged galaxies in A2744, producing 188 images in the cluster core (Mahler et al. 2018; Richard et al. 2021). This list was then recently refined to a secure, purely spectroscopic, sample by Bergamini et al. (2022). For our SL model, we use this secure spectroscopic sample of 90 multiple images belonging to 30 sources to constrain the main cluster core and refer the reader to Bergamini et al. (2022) (Tab. A.1) for a complete list of images and redshifts. To this we add the triply-imaged Zitrin et al. (2014) $z \sim 10$ object which was recently confirmed with JWST/NIRSpec spectroscopy at $z_{\text{spec}} \approx 9.76$ (Roberts-Borsani et al. 2022). We also identify a notable triply imaged dropout system at $z \sim 7 - 8$. Two of its images were previously reported in HFF high-redshift samples (Atek et al. 2014, 2015) and

identified as a photometric multiple image system in Mahler et al. (2018), system 53. The new UNCOVER data now not only reveal a third image to this system but together with the SL model also help us further to confirm its high-redshift nature. Furthermore, in the JWST observations the object appears to be extremely red and compact with a point-like morphology, suggesting it is potentially an obscured Active Galactic Nucleus (AGN; Furtak et al. 2022). Note that this new image was identified after constructing the current lens model and will therefore only be included in future versions released in future UNCOVER data releases.

The new ultra-deep UNCOVER imaging of A2744 reveals spectacular new strongly lensed multiple image systems in the northern and north-western extensions of the cluster. While these extended sub-structures are known from X-ray and WL analyses (Merten et al. 2011; Medezinski et al. 2016; Jauzac et al. 2016), they have so far not yet been confirmed to be dense enough to produce clear SL multiple images. Using the UNCOVER mosaics (see section 2.1), we

identify 17 new multiple image systems and candidate systems in the north-western and one in the northern sub-structure of the cluster in a by-eye search considering their color, visual aspect, relative geometric position, and parity. The new systems are listed and summarized in Tab. 1 and can be seen in Figs. 1 and 2 for the north-western and northern sub-structures. For systems that lack clear point-like features, we identify locations which show other unique features repeating in all counter images, such as e.g. places where the arc gets thicker or thinner, and use these as approximate image positions. The northern sub-cluster has only one clearly identified multiple image system, system 78. Note that we continue from the numbering scheme of Mahler et al. (2018), which was also perpetuated in Bergamini et al. (2022), i.e. we start at 65. Some of these multiple image systems, in particular systems 65, 71 and 78, present several sub-clumps in the JWST imaging, each of which can be used as an independent source in the SL modeling. Taking these into account, we identify a total of 75 new multiple images and image candidates in the north-western and northern sub-structures of A2744. Note that we do not use candidate multiple images, marked “c” in Tab. 1, in the lens model (see section 3.4).

Some of these new multiply imaged galaxies are of particular interest for other studies. For example, the four relatively bright red systems 66 to 69 and the fainter candidate system c79 (see Fig. 1) are completely invisible in the HST data but all have well-constrained photometric redshifts in the preliminary UNCOVER stellar population analysis (see section 2.1) $z_{\text{phot}} \approx 2.2 - 2.5$. This hints as to their probably very dusty nature and their apparent spatial proximity could indicate an overdensity at $z \sim 2.5$. Indeed, the JWST has already revealed a population of such red galaxies around the cosmic noon and even up to the epoch of cosmic reionization (e.g. Nonino et al. 2023; Fudamoto et al. 2022; Nelson et al. 2023; Barrufet et al. 2023; Zavala et al. 2023; Naidu et al. 2022; Glazebrook et al. 2023), similarly to these galaxies. Systems 68 and 69 each show a relatively bright radial image close to the north-western BCG2, as can also be seen in Fig. 1, which are of particular value to constrain the mass distribution of that cluster galaxy. We have furthermore tentatively identified a candidate multiply imaged high-redshift source, system c80, which shows various multiply imaged clumps. These images show flux in the UNCOVER bands, i.e. in F115W and red-ward, but are invisible in the HST filters which could mean that they are F814W-dropouts at $z \sim 7 - 8$. This is also supported by our lens model (see the high-redshift critical curve in Fig. 1) presented in section 4. Note however that the BUFFALO coverage in this part of the cluster is much shallower than the central HFF observations such that a low-redshift solution cannot be ruled out at this stage. We will therefore need spectroscopic observations of this object with JWST/NIRSpec to accurately determine its redshift and perhaps multiply imaged nature.

3.4 Model setup

Since A2744 is known to be a complex merging cluster, we follow the previously published SL models (e.g. Jauzac et al. 2015; Mahler et al. 2018; Bergamini et al. 2022) and place two PIEMD DM halos in the cluster core, initially centered on the two BCGs but with a free center position that is nonetheless limited to the vicinity ($\lesssim 3''$) of the BCGs. In addition, we leave the weights of the two BCGs free as well as those of several other galaxies situated close to multiple images (see Fig. 4). For BCG1 (see section 3.2) we also leave the ellipticity parameters free but fix them to the SExtractor-measured values for BCG2.

In order to model the newly discovered SL structures in the north-

west and in the north (see sections 3.2 and 3.3), we place two PIEMD halos in the north-western sub-structure, centered on the two BCGs, and another one fixed on the northern BCG. The centers of the two north-western halos are left free within $3''$ of their respective BCG. We also allow for the ellipticity parameters, weight and the core radius of the NW-BCG2 to vary since it lies very close to the radial images of systems 68 and 69. A cluster galaxy next to images 68.2 and 69.2 is also left with a free weight (see Fig. 1). Finally, we fix the value of the reference galaxy core radius in eq. (5) to $r_{\text{core},\star} = 0.2$ kpc, similar to other SL works (e.g. Richard et al. 2014). Such values, namely $r_{\text{core},\star} = 0.2$ kpc, are typical of elliptical galaxies (e.g. Wallington & Narayan 1993).

Our SL model is constrained with a total of 135 multiple images, 92 of which have spectroscopic redshifts and are situated in the cluster core as detailed in section 3.3. Among the remaining images, 37 lie in the north-western extension and 6 in the northern sub-structure. For all systems with available spectroscopic redshifts, the redshift is fixed to the measured one in the model. In addition, as can be seen in Tab. 1, systems 66 to 69 and system 72 have relatively well-constrained photometric redshifts. We therefore leave these redshifts as free parameters in the model but limit them to the 97.5% ranges of their photometric redshifts, which are relatively narrow ($\Delta z \lesssim 0.4$). All other source redshifts are left free to vary between $z_s = 0.8$ and $z_s = 10$. Note that no parity information is used in this model.

The model is optimized using a Monte-Carlo Markov Chain (MCMC) analysis in two steps: First by running ~ 150 relatively short chains of several thousand steps each to explore the parameter space, derive the covariance matrix encoding the correlations between the different parameters, and potentially to approach the global minimum of the source plane χ^2 -function defined as

$$\chi^2 = \sum_i \frac{(\vec{\beta}_i - \vec{\beta}_0)^2}{\mu_i^2 \sigma_i^2} + \sigma_p p, \quad (8)$$

where $\vec{\beta}_i$ represents the source position of each multiple image, $\vec{\beta}_0$ the common modeled barycenter source position of the images belonging to the same system, and μ_i and σ_i the magnification and positional uncertainty of each multiple image. The second term represents the forced parities where p is the number of images modeled with the wrong parity and σ_p a constant factor to add to the χ^2 for each wrong parity. Note that we perform the minimization in the source plane which in principle should perform just as well as a lens plane minimization (Keeton 2010), as is also evident by the quality of some HFF SL models that were built using a source plane minimization, but has the advantage of being significantly faster. The result from this multi-chain first step is then further refined with two or more long MCMC chains, each of several $\sim 10^4$ steps and a decreasing “temperature”, enabling in practice some annealing. We assume a positional uncertainty of $\sigma_i = 0.5''$ for all multiple images used as constraints. We can also evaluate the χ^2 in the lens plane, defined as

$$\chi^2 = \sum_i \frac{(\vec{\theta}_i - \vec{\theta}_{i,\text{model}})^2}{\sigma_i^2} + \sigma_p p, \quad (9)$$

where $\vec{\theta}_i$ is the observed position of the i -th image and $\vec{\theta}_{i,\text{model}}$ its predicted position, which should be roughly similar to the source-plane χ^2 (Keeton 2010).

Note that although the nominal positional uncertainty adopted for the multiple images in the χ^2 calculations in (8) and (9) is taken as $0.5''$, the statistical uncertainties of the resulting model param-

ters are calculated from an MCMC chain that is run with effectively $\sim 3.5\times$ that value, $1.76''$. In practice, this is done by adopting a higher temperature when estimating the parameter uncertainties than the nominal one used in the minimization of the final chain, which we have found to be representative of the true parameter uncertainties. Note that this only affects the uncertainty estimate of the parameters and not the best-fit value or the χ^2 minimization. This factor was estimated previously on mock clusters by repeating the minimization 50 times while perturbing all multiple image positions with a Gaussian of width $\sigma = 0.5''$ in both coordinates in order to assess how the multiple images' positional uncertainty affects the parameter posterior distribution.

4 RESULTS AND DISCUSSION

Our resulting SL model of A2744 has a final *lens plane* χ^2 (9) of $\chi^2 = 234$ and an average, lens-plane image reproduction RMS of $0.66''$. Our model has 161 SL constraints (i.e. 2×135 , the number of images, minus 2×46 , the number of systems used in the modeling, minus 15, the number of systems whose redshift was left free, after equation 1 in Kneib et al. 1993), and 61 free parameters, which results in 102 degrees of freedom. This nominally leads to a reduced lens plane χ^2 of $\simeq 2.3$, i.e. somewhat above but of order unity. For comparison, our image reproduction RMS is of the same order as quoted for the Mahler et al. (2018) model ($0.67''$) and $1.8\times$ higher than the value quoted for the Bergamini et al. (2022) model ($0.37''$). Note however that we include a multitude (15) of new multiple image systems without precise redshift measurements to constrain the outer sub-structures, as opposed to their secure purely spectroscopic sample in the cluster core. Indeed, e.g. Johnson & Sharon (2016) found that the RMS-scatter in the lens plane may degrade when less spectroscopic systems are used for the modeling. Moreover, caution should be taken when comparing RMS values, which may be calculated somewhat differently in different works or between different modelers.

We show the critical curves for sources at redshifts $z_s = 1.6881$ and $z_s = 10$ in Fig. 4. The redshift $z_s = 1.6881$ corresponds to the redshift of system 1 (Mahler et al. 2018) and represents the redshift to which the distance ratios are normalized in our model. More detailed zoomed-in versions on the extended sub-structures in the north-west and in the north can be seen in Figs. 1 and 2, respectively. The figure illustrates how the inclusion of the northern and north-western extensions increases the total critical area of A2744 by a factor ~ 1.5 . We indeed find a total critical area of $A_{\text{crit}} = 0.67 \text{ arcmin}^2$ which translates into an effective Einstein radius of $\theta_E = 27.7'' \pm 2.8''$ for a source at $z_s = 2$. The total cluster mass enclosed by those curves is $M(< \theta_E) = (1.07 \pm 0.15) \times 10^{14} M_\odot$. In particular the area between the main cluster and north-western extension forms a high-magnification 'bridge' where the magnification remains $\mu \geq 4$ for sources at $z_s = 10$ as can be seen in Fig. 5. Individually, the main cluster has a $z_s = 2$ critical area of $A_{\text{crit,main}} = 0.47 \text{ arcmin}^2$ ($\theta_{E,\text{main}} = 23.2'' \pm 2.3''$) comprising a mass of $M(< \theta_{E,\text{main}}) = (7.7 \pm 1.1) \times 10^{13} M_\odot$. The northern and north-western substructures each have critical areas of $A_{\text{crit,N}} = 0.05 \text{ arcmin}^2$ ($\theta_{E,N} = 7.4'' \pm 0.7''$) and $A_{\text{crit,NW}} = 0.15 \text{ arcmin}^2$ ($\theta_{E,NW} = 13.1'' \pm 1.3''$), enclosing masses of $M(< \theta_{E,N}) = (0.8 \pm 0.1) \times 10^{13} M_\odot$ and $M(< \theta_{E,NW}) = (2.2 \pm 0.3) \times 10^{13} M_\odot$ respectively. In the above we adopt nominal errors of 10% and 14% for the effective Einstein radii and enclosed masses, respectively, which encompass the typical systematic scatter of these values between different models (e.g. Zitrin et al. 2015). The statistical errors that we obtain from our model are

smaller, of the order $\sim 2 - 3\%$ for the effective Einstein radius and $\sim 5\%$ for the enclosed total mass.

The median PIEMD parameters of the five DM halos in our model are listed in Tab. 2. Note that the northern halo seems to be unexpectedly massive given the apparent dearth of multiple image systems in that region (see section 3.3). This particular sub-structure is therefore probably poorly constrained due to its lack of many multiple images and spectroscopic redshifts to anchor the model in that region. Because of that, we surmise that this halo in particular might be overestimated in our model. Our results in the main cluster agree well with Mahler et al. (2018) and Bergamini et al. (2022) which is unsurprising since we use a similar setup and rely on the same set of multiple images and spectroscopic redshifts to constrain this region of the cluster. In particular, the Mahler et al. (2018) model, which achieved a similar lens plane RMS as ours (see above), finds an effective Einstein radius of $\simeq 23.9''$ for $z_s = 4$ (given in Richard et al. 2021) in the main cluster core where our model yields $\theta_{E,\text{main}} = 26.2'' \pm 2.6''$ for the same source redshift. These two models therefore concur within the uncertainties. We also refer the reader to Fig. 1 in Roberts-Borsani et al. (2022) where we overlaid the $z_s = 10$ critical curves of our preliminary main cluster core model alongside those of the Zitrin et al. (2014) and Bergamini et al. (2022) models. Furthermore, we find a total cluster mass of $M(r < 200 \text{ kpc}) = (1.60 \pm 0.22) \times 10^{14} M_\odot$ within 200 kpc of BCG2 (see Fig. 4) which also agrees with the value found in Bergamini et al. (2022) within the uncertainties. The two models by Mahler et al. (2018) and Bergamini et al. (2022) also include the extended sub-structures in the north and the north-west based on the previous predictions from WL and the BUFFALO HST imaging, but do not constrain them directly due to the lack on SL features in that region prior to the UNCOVER imaging. With the new multiple images identified in this study, however, we find much less massive DM halos than Mahler et al. (2018) and slightly less massive halos than Bergamini et al. (2022) in these structures. In particular, the northern DM halo has a much lower mass in our model (see Tab. 2) than in both Mahler et al. (2018) and Bergamini et al. (2022) and even so, judging by the single multiply imaged system found around that clump (see Fig. 2), we suspect that the mass of this sub-structure is overestimated, as explained above.

The resulting parameters for the BCGs and cluster galaxies left free in our model (see section 3.4) are listed in Tab. 3. We find the reference galaxy of (fixed) luminosity $M_\star = -21.05$ (in absolute magnitudes) to have a velocity dispersion $\sigma_{v,\star} = 117 \pm 4 \frac{\text{km}}{\text{s}}$ and a truncation radius $r_{\text{cut},\star} = 57 \pm 9 \text{ kpc}$. The median scaling relations eqs. (4)-(6) are $\lambda = 0.40^{+0.02}_{-0.01}$, $\beta = 0.77^{+0.05}_{-0.02}$ and $\alpha = 0.63^{+0.01}_{-0.02}$. Note that these seem to work very well, as is evident by the fact that multiple image systems that lie very close to cluster galaxies, such that their lensing signal is dominated by them (e.g., systems 65 and 71; see Fig. 1), are exceptionally well reproduced by our model. In addition, the λ -parameter agrees perfectly with the value of $\simeq 0.4$ measured in Bergamini et al. (2022) from the internal stellar kinematics of cluster galaxies (Bergamini et al. 2019, 2021). While our result for the power-law index of the scaling relation for the truncation radius disagrees with the $\alpha \simeq 0.41$ kinematic measurement in Bergamini et al. (2022), we also find a much higher $r_{\text{cut},\star}$ amplitude in our model despite our reference galaxy being fainter. Using eq. (3), we compute the total mass of our reference galaxy $M_{\text{tot},\star} = (5.7 \pm 1.8) \times 10^{11} M_\odot$ which, together with its luminosity $L_\star = 2.2 \times 10^{10} L_\odot$, agrees with typical halo mass to luminosity relations (e.g. Vale & Ostriker 2004). Finally, the median redshifts for the multiple image systems optimized in this model, i.e. all the new ones identified in UNCOVER imaging of the extended structures, are given in Tab. 1. Note that in the case of

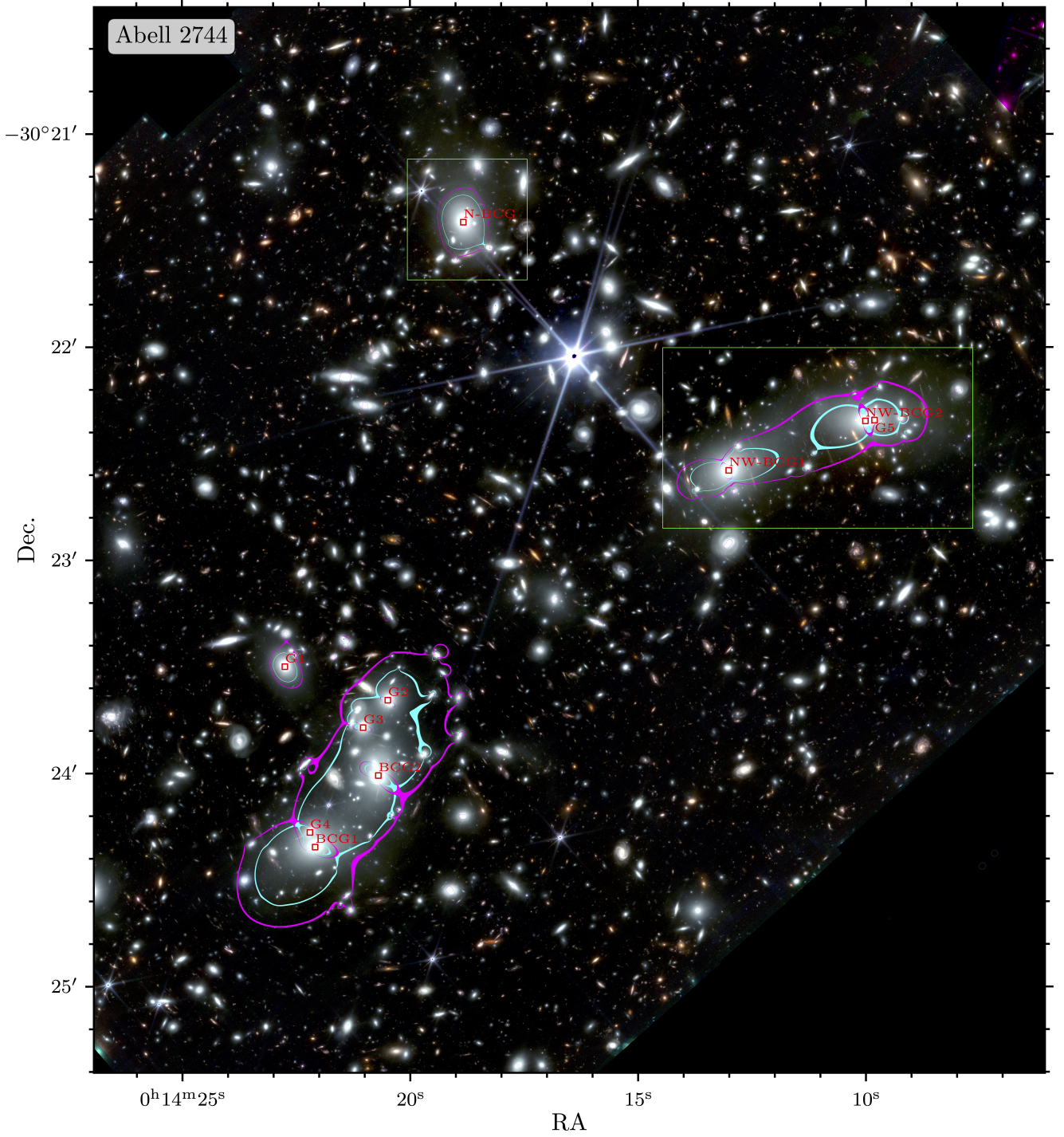


Figure 4. A $4.5' \times 5.0'$ cutout of an UNCOVER/NIRCam composite-color image of A2744 in the same filter configuration as in Figs. 1 and 2. Cluster galaxies left free to vary in our SL model (see section 3.4 and Tb. 3) are shown in red. Overlaid we show the critical curves of our SL model for source redshifts $z_s = 1.6881$ (corresponding to system 1) and $z_s = 10$ in blue and purple respectively as in Fig 1. The area between the main cluster and the north-western sub-structure in particular has high magnifications of order $\mu \gtrsim 4$ for sources at $z_s = 10$ (see Fig. 5). The green rectangles outline the fields shown in more detail in Figs. 1 and 2. Note, a vectorized full UNCOVER resolution ($0.04''/\text{pix}$) version of this figure is available in the online supplemental material of this paper.

Table 2. Median DM halo PIEMD parameters, defined in eqs. (2) and (7) in section 3.1, and their 1σ -errors for our SL model of A2744.

Halo	RA	Dec.	ϵ	θ [Degrees]	σ_v [$\frac{\text{km}}{\text{s}}$]	r_{core} [kpc]
<i>Main cluster core</i>						
Main-1	00:14:22.17 $^{+0.01}_{-0.01}$	-30:24:18.32 $^{+0.31}_{-0.22}$	0.41 $^{+0.02}_{-0.03}$	45 $^{+4}_{-1}$	681 $^{+34}_{-16}$	23 $^{+4}_{-2}$
Main-2	00:14:20.80 $^{+0.03}_{-0.01}$	-30:24:00.85 $^{+0.29}_{-0.64}$	0.45 $^{+0.01}_{-0.02}$	73 $^{+3}_{-2}$	807 $^{+45}_{-72}$	67 $^{+8}_{-20}$
<i>North-western extension</i>						
North-West-1	00:14:13.16 $^{+0.02}_{-0.01}$	-30:22:35.65 $^{+0.34}_{-0.13}$	0.55 $^{+0.02}_{-0.02}$	19 $^{+3}_{-7}$	407 $^{+21}_{-18}$	5 $^{+1}_{-1}$
North-West-2	00:14:10.08 $^{+0.03}_{-0.01}$	-30:22:19.90 $^{+0.22}_{-0.38}$	0.18 $^{+0.02}_{-0.04}$	-8 $^{+3}_{-5}$	906 $^{+30}_{-73}$	62 $^{+4}_{-16}$
<i>Northern extension</i>						
North	00:14:18.83	-30:21:24.84	0.10 $^{+0.02}_{-0.02}$	-73 $^{+2}_{-5}$	486 $^{+17}_{-16}$	2 $^{+2}_{-1}$

Note. – *Column 1:* DM halo designation – *Columns 2 and 3:* Right ascension and declination. The northern halo is fixed onto its BCG’s position (see section 3.4). – *Column 4:* Ellipticity defined as $\epsilon = \frac{b-a}{a+b}$ where a and b are the semi-major and -minor axes respectively. – *Column 5:* Position angle, counter-clockwise with respect to the east-west axis. – *Column 6:* Velocity dispersion of the PIEMD profile. – *Column 7:* Core radius of the PIEMD profile.

Table 3. Median dPIE parameters, defined in eqs. (1) and (2) in section 3.1, and their 1σ -errors of the BCGs and the galaxies left free in our SL model of A2744.

Galaxy	RA ^a	Dec. ^a	σ_v [$\frac{\text{km}}{\text{s}}$]	r_{core} [kpc]	r_{cut} [kpc] ^b	ϵ	θ [Degrees]	M_{tot} [$10^{12} M_{\odot}$]
<i>Main cluster core</i>								
BCG1	00:14:22.09	-30:24:20.73	233 $^{+30}_{-15}$	0.525 $^{+0.033}_{-0.016}$ b	126 \pm 20	0.14 \pm 0.02	31 $^{+3}_{-3}$	4.98 $^{+2.01}_{-1.67}$
BCG2	00:14:20.70	-30:24:00.59	311 $^{+26}_{-23}$	0.499 $^{+0.029}_{-0.015}$ b	121 \pm 19	0.09 ^a	-67 ^a	8.52 $^{+3.00}_{-2.96}$
G1	00:14:22.75	-30:23:29.94	341 $^{+23}_{-19}$	0.469 $^{+0.026}_{-0.013}$ b	115 \pm 18	-	-	9.73 $^{+3.27}_{-3.18}$
G2	00:14:20.49	-30:23:39.38	225 $^{+16}_{-22}$	0.364 $^{+0.014}_{-0.007}$ b	94 \pm 14	-	-	3.44 $^{+1.16}_{-1.24}$
G3	00:14:21.03	-30:23:47.11	200 $^{+16}_{-16}$	0.326 $^{+0.010}_{-0.005}$ b	86 \pm 13	-	-	2.48 $^{+0.86}_{-0.85}$
G4	00:14:22.20	-30:24:16.61	161 $^{+30}_{-16}$	0.287 $^{+0.007}_{-0.003}$ b	77 \pm 12	-	-	1.45 $^{+0.70}_{-0.53}$
<i>North-western extension</i>								
NW-BCG1	00:14:13.01	-30:22:34.72	201 $^{+9}_{-8}$ b	0.562 $^{+0.037}_{-0.019}$ b	134 \pm 21	0.07 ^a	38 ^a	3.92 $^{+1.26}_{-1.25}$
NW-BCG2	00:14:10.01	-30:22:20.79	218 $^{+18}_{-23}$	0.614 $^{+0.073}_{-0.050}$ b	126 \pm 19	0.16 \pm 0.01	-16 $^{+2}_{-6}$	4.36 $^{+1.52}_{-1.63}$
G5	00:14:09.81	-30:22:20.56	108 $^{+6}_{-7}$	0.095 $^{+0.007}_{-0.003}$ b	31 \pm 5	-	-	0.27 $^{+0.09}_{-0.09}$
<i>Northern extension</i>								
N-BCG	00:14:18.83	-30:21:24.83	196 $^{+9}_{-8}$ b	0.533 $^{+0.034}_{-0.017}$ b	128 \pm 20	0.14 ^a	-70 ^a	3.56 $^{+1.14}_{-1.14}$

^a Fixed to the SExtractor-measured values (see section 3.2).

^b Scaled to the galaxy luminosity using the relations (4)-(6).

Note. – *Column 1:* Galaxy designation. – *Columns 2 and 3:* Right ascension and declination. – *Column 4:* Velocity dispersion of the dPIE profile. – *Column 5:* Core radius of the dPIE profile. – *Column 6:* Truncation radius of the dPIE profile. – *Column 7:* Ellipticity defined as $\epsilon = \frac{b-a}{a+b}$ where a and b are the semi-major and -minor axes respectively. All non-BCG-type galaxies are assumed to be spherical (see section 3.1). – *Column 8:* Position angle, counter-clockwise with respect to the east-west axis. – *Column 9:* Total mass of the dPIE profile computed from the model parameters following eq. 3.

multiple image systems that split into several sub-systems, we report the median redshift of the best reproduced sub-system.

We make our SL model publicly available on the UNCOVER website under: <https://jwst-uncover.github.io/DR1.html#LensingMaps>. The release comprises $7.6' \times 7.6'$ deflection maps, α_x and α_y , a convergence κ -map, and shear γ_1 - and γ_2 -maps, which cover the entire UNCOVER NIRCcam footprint. We provide maps both in NIRCcam UNCOVER pixel scale of $0.04''/\text{pix}$, and in lower $0.1''/\text{pix}$ resolution for the best-fit model and a range of low-resolution maps drawn from the final MCMC chain for error computation. The release also contains a set of magnification maps for various source redshifts.

The deep JWST imaging and SL mass model presented here for the first time fully reveal the SL power of the massive northern

clumps ($\sim 3'$ north and north-west of the main cluster core; see Fig. 4) in A2744. These were previously only constrained with WL measurements (Merten et al. 2011; Medezinski et al. 2016; Jauzac et al. 2016) which are much less sensitive to the small-scale mass distribution than the SL regime. While the WL analyses did indeed predict the three distinct northern sub-halos that we also model, we are now able to pinpoint their exact positions thanks to the more sensitive SL signal (see Tab. 2) and can confirm the halo positions to coincide with the three BCG-type galaxies identified in the north of A2744 (see section 3.2). Because of the different sensitivities of the SL and WL regimes, a direct quantitative comparison between the derived total masses is not possible. We nevertheless find the two northern sub-structures to be somewhat less massive than predicted by the WL, in particular by ~ 1 order of magnitude compared to

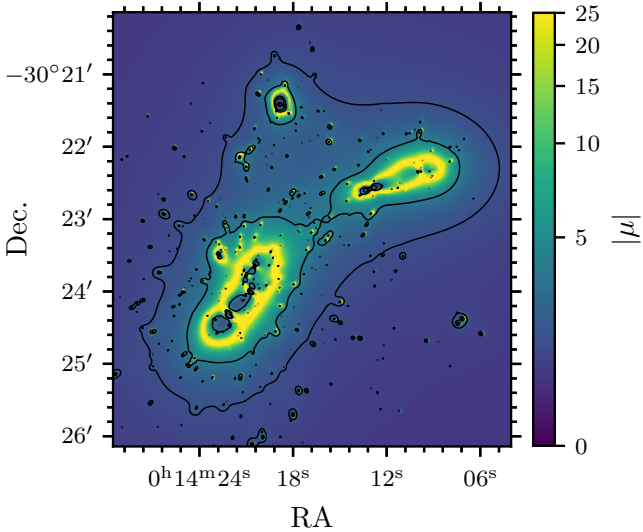


Figure 5. Magnification map of our final model for a source redshift $z_s = 10$. The black contours represent magnification thresholds of $\mu = 2$ and $\mu = 4$. The area between the main cluster and the extended sub-structures forms contiguous sheet of $\mu > 2$ which goes up to $\mu \gtrsim 4$ between the main cluster and the north-western extension.

Jauzac et al. (2016). Note that all three WL studies predict an additional massive sub-halo west of the cluster core (Merten et al. 2011; Medezinski et al. 2016; Jauzac et al. 2016), which lies just outside of the UNCOVER field-of-view. The extended HST data do not show a prominent cluster galaxy overdensity in that vicinity, even though there are two bright cluster galaxies at the position where Merten et al. (2011) predict the western sub-clump. We do not find any SL features in this region that could hint at an additional dense SL halo. That being said, the BUFFALO HST data in this region are shallower than the central HFF observations and possible faint SL features might therefore not be detected. Our model, however, does not require an external shear component (in early tries, introducing a freely optimized external shear free did not improve the model and the resulting external shear was very low), so if there is an additional sub-halo, it cannot be massive enough to significantly affect the SL signal of the multiple images identified in A2744 thus far. In addition, both Medezinski et al. (2016) and Jauzac et al. (2016) predict another sub-structure in the north-east of the main cluster but disagree on its position. The UNCOVER NIRCcam data reveal a small overdensity of apparent cluster galaxies a few arc-seconds from the Jauzac et al. (2016) predicted centroid which seems to contain one prominent candidate galaxy-galaxy SL system. There is not sufficient HST coverage of this region however to robustly select cluster galaxies. This feature is therefore not included in the present analysis because we select the cluster galaxies based on their color around the 4000 Å-break in the HST data (see section 3.2). Future analyses should nevertheless investigate this system with spectroscopy to see if an additional sub-halo is needed in the north-east of the cluster. The most prominent sub-structure in A2744 by far is the north-western extension as can be seen in Figs. 1, 4 and 5. We note that its position and morphology align well with the cosmic filament direction found by Jauzac et al. (2016). Future studies combining both WL and SL modeling will be able to further examine these conclusions and expand on them. Given the wide field-of-view and unparalleled spatial resolution of the UNCOVER imaging, it will be particularly inter-

esting to see how an UNCOVER-based WL analysis would agree or disagree with our SL-based findings.

The main limitation of our model is that, unlike the secure multiple images around the main cluster core (Bergamini et al. 2022), the newly discovered images around the two northern sub-structures do not have spectroscopic redshifts, which makes the SL model somewhat less secure in that region. Indeed, low numbers of spectroscopic redshift constraints have been found to strongly affect e.g. magnification measurements (e.g. Meneghetti et al. 2017; Acebron et al. 2017, 2018). However, the multitude of systems together with the relatively tightly constrained photometric redshifts for some of them (see Tab. 1) allow us to still obtain a relatively accurate solution as demonstrated by the low lens plane RMS achieved by our model. More robust modeling of these structures will however require spectroscopic redshift measurements of the new SL features detected in UNCOVER, either with VLT/MUSE for the brighter and bluer images or with JWST/NIRSpec for the fainter and redder ones such as our candidate $z \sim 2.5$ overdensity (see section 3.3). The UNCOVER NIRSpec follow-up observations, scheduled for July 2023, for example will be of great use in this regard.

The newly established SL sub-structure in the north of A2744 also now allows us to more precisely estimate the magnification of background sources in and around the cluster field since these have been found to be significantly affected by massive structures in the outskirts of simulated lensing clusters (e.g. Meneghetti et al. 2017; Acebron et al. 2017). Because of its unprecedented depth, large field-of-view and numerous ancillary data sets (see Bezanson et al. 2022), the JWST UNCOVER field represents one of the prime fields for galaxy studies across the observable Universe. This is emphasized further by the relatively large high-magnification ($\mu \gtrsim 4$) area spanned by the cluster sub-structures, in particular the main cluster and the north-western extension (see Fig. 5), as discussed above. Studies of galaxies in this field will therefore require accurate gravitational magnification measurements such as provided by our SL model presented here and its subsequent versions.

5 CONCLUSION

We present a new parametric SL model of the galaxy cluster A2744 based on hitherto unknown multiple image systems in the northern and north-western extensions of the cluster. Thanks to the ultra-deep and wide coverage of the JWST/NIRCcam imaging taken for the UNCOVER program, we are able to identify numerous new multiple images and candidates in the two northern sub-structures of the cluster. Since no spectroscopic redshifts are available for these multiple image systems, we compile a relatively secure sub-set of SL constraints based on position, parity and photometric redshifts, as well as support by preliminary lens models. These new SL constraints are then combined with the Bergamini et al. (2022) spectroscopic sample and a now confirmed $z_{\text{spec}} = 9.76$ system (Roberts-Borsani et al. 2022) in the main cluster, forming a total sample of 135 multiple images used in our model. The SL model is constructed with an updated version of the parametric lensing mass modeling code by Zitrin et al. (2013a,b); Zitrin (2021) and comprises five large-scale cluster DM halos, five BCGs and a total of 421 cluster galaxies. Our final model reproduces the multiple images with a *lens plane* RMS of $0.66''$.

Our main results are the following:

- The UNCOVER imaging reveals two massive sub-structures ($\sim 3'$) north and north-west of the central core of A2744. We uncover 75 new strongly lensed multiple images and multiple image candidates

belonging to 17 sources around these structures, and establish them as prominent SL systems for the first time. These new multiple image systems include a potential overdensity of bright and red (i.e. HST-dark) sources at $z_{\text{phot}} \sim 2.5$ behind the north-western sub-structure. We use 43 of these new multiple images to constrain our SL model in these regions.

- Our model yields a total critical area of $A_{\text{crit}} = 0.67 \text{ arcmin}^2$ for A2744 (assuming a source redshift $z_s = 2$) which implies an effective Einstein radius of $\theta_E = 27.7'' \pm 2.8''$ enclosing a total projected mass of $M(< \theta_E) = (1.07 \pm 0.15) \times 10^{14} M_{\odot}$. This corresponds to a total cluster mass of $M(r < 200 \text{ kpc}) = (1.60 \pm 0.22) \times 10^{14} M_{\odot}$ within 200 kpc of BCG2.

- The main cluster core has an effective $z_s = 2$ Einstein radius $\theta_{E,\text{main}} = 23.2'' \pm 2.3''$ enclosing $M(< \theta_{E,\text{main}}) = (7.7 \pm 1.1) \times 10^{13} M_{\odot}$ and agrees well with previous SL models of A2744.

- The northern and north-western sub-clumps have effective $z_s = 2$ Einstein radii of $\theta_{E,N} = 7.4'' \pm 0.7''$ and $\theta_{E,NW} = 13.1'' \pm 1.3''$, enclosing total masses of $M(< \theta_{E,N}) = (0.8 \pm 0.1) \times 10^{13} M_{\odot}$ and $M(< \theta_{E,NW}) = (2.2 \pm 0.3) \times 10^{13} M_{\odot}$, respectively. These substructures are somewhat less massive than in previous SL studies in which these DM sub-halos were not directly constrained, however.

- Including the two northern sub-structures in the SL model effectively increased the critical area of the cluster by a factor ~ 1.5 . We in particular find an extended high-magnification (e.g. $\mu \gtrsim 4$ for $z_s = 10$) area between the three cluster structures in the lens plane.

- Our SL-constrained sub-structures broadly agree with WL analysis results of A2744 but find much lower masses for the individual DM halos.

Our lens model is made available to the community, together with the public UNCOVER data release⁵ (Bezanson et al. 2022). Future studies will need to measure spectroscopic redshifts of the newly discovered SL features in the outskirts of A2744 and include WL constraints to more robustly probe the complete DM sub-structure of the cluster. A part of that can be done with JWST UNCOVER data, including the upcoming NIRSpec spectroscopy. Our model will be updated in future versions with new constraints when they become available.

ACKNOWLEDGEMENTS

We thank the anonymous referee for their useful comments and feedback that greatly helped to improve the completeness and clarity of this paper. LF and AZ would like to thank Ashish K. Meena for useful comments and discussions.

LF and AZ acknowledge support by Grant No. 2020750 from the United States-Israel Binational Science Foundation (BSF) and Grant No. 2109066 from the United States National Science Foundation (NSF). The BGU lensing group further acknowledges support by the Ministry of Science & Technology, Israel. HA acknowledges support from CNES (Centre National d'Etudes Spatiales). RB acknowledges support from the Research Corporation for Scientific Advancement (RCSA) Cottrell Scholar Award ID No.: 27587. PD acknowledges support from the NWO grant 016.VIDI.189.162 ("ODIN") and from the European Commission's and University of Groningen's CO-FUND Rosalind Franklin program. The Cosmic Dawn Center is funded by the Danish National Research Foundation (DNRF) under grant #140. Support for the program JWST-GO-02561 was provided through a grant from the STScI under NASA contract NAS 5-03127.

⁵ <https://jwst-uncover.github.io/DR1.html>

This work is based on observations obtained with the NASA/ESA/CSA JWST and the NASA/ESA *Hubble Space Telescope* (HST), retrieved from the Barbara A. Mikulski Archive for Space Telescopes (MAST) at the *Space Telescope Science Institute* (STScI). STScI is operated by the Association of Universities for Research in Astronomy, Inc. under NASA contract NAS 5-26555. This work is also based on observations made with ESO Telescopes at the La Silla Paranal Observatory which are publicly available on the ESO Science Archive Facility.

This research made use of *Astropy*,⁶ a community-developed core Python package for Astronomy (Astropy Collaboration et al. 2013; Price-Whelan et al. 2018) as well as the packages *NumPy* (van der Walt et al. 2011), *SciPy* (Virtanen et al. 2020), *Matplotlib* (Hunter 2007) and the MAAT Astronomy and Astrophysics tools for MATLAB (Ofek 2014).

DATA AVAILABILITY

The raw JWST and HST data used in this work are publicly available on the MAST and the reduced UNCOVER JWST and HST mosaics and catalogs are part of the public data release by the UNCOVER team⁷ (Bezanson et al. 2022; Weaver et al. 2023). The spectroscopic redshifts were measured by Mahler et al. (2018), Bergamini et al. (2022) and Roberts-Borsani et al. (2022) based on data that are publicly available on the ESO Science Archive⁸ and the GLASS website⁹.

REFERENCES

- Abell G. O., Corwin Jr. H. G., Olowin R. P., 1989, *ApJS*, **70**, 1
- Acebron A., Jullo E., Limousin M., Tilquin A., Giocoli C., Jauzac M., Mahler G., Richard J., 2017, *MNRAS*, **470**, 1809
- Acebron A., et al., 2018, *ApJ*, **858**, 42
- Allen S. W., 1998, *MNRAS*, **296**, 392
- Amoura Y., Drakos N. E., Berrouet A., Taylor J. E., 2021, *MNRAS*, **508**, 100
- Asencio E., Banik I., Kroupa P., 2021, *MNRAS*, **500**, 5249
- Astropy Collaboration et al., 2013, *A&A*, **558**, A33
- Ata M., Lee K.-G., Vecchia C. D., Kitaura F.-S., Cucciati O., Lemaux B. C., Kashino D., Müller T., 2022, *Nature Astronomy*, **6**, 857
- Atek H., et al., 2014, *ApJ*, **786**, 60
- Atek H., et al., 2015, *ApJ*, **800**, 18
- Atek H., Richard J., Kneib J.-P., Schaerer D., 2018, *MNRAS*, **479**, 5184
- Bacon R., et al., 2010, in McLean I. S., Ramsay S. K., Takami H., eds, *Society of Photo-Optical Instrumentation Engineers (SPIE) Conference Series Vol. 7735, Ground-based and Airborne Instrumentation for Astronomy III*, p. 773508, doi:10.1117/12.856027
- Barbary K., 2016, *Journal of Open Source Software*, **1**, 58
- Barbary K., 2018, SEP: Source Extraction and Photometry, *Astrophysics Source Code Library*, record ascl:1811.004 (ascl:1811.004)
- Barrufet L., et al., 2023, *MNRAS*, **522**, 449
- Bergamini P., et al., 2019, *A&A*, **631**, A130
- Bergamini P., et al., 2021, *A&A*, **645**, A140
- Bergamini P., et al., 2022, arXiv e-prints, p. arXiv:2207.09416
- Bertin E., Arnouts S., 1996, *Astronomy and Astrophysics Supplement Series*, **117**, 393
- Bezanson R., et al., 2022, arXiv e-prints, p. arXiv:2212.04026
- Bhatawdekar R., Conselice C. J., Margalef-Bentabol B., Duncan K., 2019, *MNRAS*, **486**, 3805

⁶ <http://www.astropy.org>

⁷ <https://jwst-uncover.github.io>

⁸ <https://archive.eso.org/scienceportal/home>

⁹ <https://glass.astro.ucla.edu>

- Böker T., et al., 2023, *PASP*, **135**, 038001
- Borgani S., Guzzo L., 2001, *Nature*, **409**, 39
- Bouwens R. J., Oesch P. A., Illingworth G. D., Ellis R. S., Stefanon M., 2017, *ApJ*, **843**, 129
- Bouwens R. J., Illingworth G., Ellis R. S., Oesch P., Paulino-Afonso A., Ribeiro B., Stefanon M., 2022, *ApJ*, **931**, 81
- Braglia F. G., Pierini D., Biviano A., Boehringer H., 2009, VizieR Online Data Catalog, [pp J/A+A/500/947](https://vizier.cfa.harvard.edu/vizier/ftp/J/A+A/500/947)
- Brammer G. B., van Dokkum P. G., Coppi P., 2008, *ApJ*, **686**, 1503
- Broadhurst T. J., Barkana R., 2008, *MNRAS*, **390**, 1647
- Broadhurst T., Umetsu K., Medezinski E., Oguri M., Rephaeli Y., 2008, *ApJ*, **685**, L9
- Caminha G. B., Suyu S. H., Mercurio A., Brammer G., Bergamini P., Acebron A., Vanzella E., 2022, *A&A*, **666**, L9
- Coe D., Bradley L., Zitrin A., 2015, *ApJ*, **800**, 84
- Coe D., et al., 2019, *ApJ*, **884**, 85
- Diego J. M., et al., 2023, *A&A*, **672**, A3
- Doyon R., et al., 2012, in Clampin M. C., Fazio G. G., MacEwen H. A., Oschmann Jacobus M. J., eds, Society of Photo-Optical Instrumentation Engineers (SPIE) Conference Series Vol. 8442, Space Telescopes and Instrumentation 2012: Optical, Infrared, and Millimeter Wave. p. 84422R, [doi:10.1117/12.926578](https://doi.org/10.1117/12.926578)
- Dubois Y., et al., 2014, *MNRAS*, **444**, 1453
- Durret F., et al., 2016, *A&A*, **588**, A69
- Ebeling H., Barrett E., Donovan D., 2004, *ApJ*, **609**, L49
- Ebeling H., Barrett E., Donovan D., Ma C.-J., Edge A. C., van Speybroeck L., 2007, *ApJ*, **661**, L33
- Ebeling H., Edge A. C., Mantz A., Barrett E., Henry J. P., Ma C. J., van Speybroeck L., 2010, *MNRAS*, **407**, 83
- Elíasdóttir Á., et al., 2007, preprint, ([arXiv:0710.5636](https://arxiv.org/abs/0710.5636))
- Ellien A., Durret F., Adami C., Martinet N., Lobo C., Jauzac M., 2019, *A&A*, **628**, A34
- Faber S. M., Jackson R. E., 1976, *ApJ*, **204**, 668
- Ferruit P., et al., 2022, *A&A*, **661**, A81
- Foley R. J., et al., 2011, *ApJ*, **731**, 86
- Fudamoto Y., Inoue A. K., Sugahara Y., 2022, arXiv e-prints, [p. arXiv:2208.00132](https://arxiv.org/abs/2208.00132)
- Furtak L. J., Atek H., Lehnert M. D., Chevillard J., Charlot S., 2021, *MNRAS*, **501**, 1568
- Furtak L. J., et al., 2022, arXiv e-prints, [p. arXiv:2212.10531](https://arxiv.org/abs/2212.10531)
- Gardner J. P., et al., 2006, Science with the James Webb space telescope. SPIE, p. 62650N, [doi:10.1117/12.670492](https://doi.org/10.1117/12.670492)
- Glazebrook K., et al., 2023, *ApJ*, **947**, L25
- González-López J., et al., 2017, *A&A*, **597**, A41
- Grillo C., et al., 2015, *ApJ*, **800**, 38
- Halkola A., Seitz S., Pannella M., 2006, *MNRAS*, **372**, 1425
- Halkola A., Seitz S., Pannella M., 2007, *ApJ*, **656**, 739
- Hatfield P. W., Laigle C., Jarvis M. J., Devriendt J., Davidzon I., Ilbert O., Pichon C., Dubois Y., 2019, *MNRAS*, **490**, 5043
- Hennawi J. F., Dalal N., Bode P., Ostriker J. P., 2007, *ApJ*, **654**, 714
- Hsiao T. Y.-Y., et al., 2022, arXiv e-prints, [p. arXiv:2210.14123](https://arxiv.org/abs/2210.14123)
- Hunter J. D., 2007, *Computing in Science & Engineering*, **9**, 90
- Ishigaki M., Kawamata R., Ouchi M., Oguri M., Shimasaku K., Ono Y., 2015, *ApJ*, **799**, 12
- Ishigaki M., Kawamata R., Ouchi M., Oguri M., Shimasaku K., Ono Y., 2018, *ApJ*, **854**, 73
- Jaffe W., 1983, *MNRAS*, **202**, 995
- Jakobsen P., et al., 2022, *A&A*, **661**, A80
- Jauzac M., et al., 2012, *MNRAS*, **426**, 3369
- Jauzac M., et al., 2015, *MNRAS*, **452**, 1437
- Jauzac M., et al., 2016, *MNRAS*, **463**, 3876
- Jauzac M., et al., 2018, *MNRAS*, **481**, 2901
- Johnson T. L., Sharon K., 2016, *ApJ*, **832**, 82
- Johnson T. L., Sharon K., Bayliss M. B., Gladders M. D., Coe D., Ebeling H., 2014, *ApJ*, **797**, 48
- Jullo E., Kneib J.-P., 2009, *MNRAS*, **395**, 1319
- Jullo E., Kneib J.-P., Limousin M., Elíasdóttir Á., Marshall P. J., Verdugo T., 2007, *New Journal of Physics*, **9**, 447
- Kartaltepe J. S., Ebeling H., Ma C. J., Donovan D., 2008, *MNRAS*, **389**, 1240
- Kawamata R., Oguri M., Ishigaki M., Shimasaku K., Ouchi M., 2016, *ApJ*, **819**, 114
- Kawamata R., Ishigaki M., Shimasaku K., Oguri M., Ouchi M., Tanigawa S., 2018, *ApJ*, **855**, 4
- Keeton C. R., 2001, arXiv e-prints, [pp astro-ph/0102341](https://arxiv.org/abs/astro-ph/0102341)
- Keeton C. R., 2010, *General Relativity and Gravitation*, **42**, 2151
- Kelly P. L., et al., 2015, *Science*, **347**, 1123
- Kelly P. L., et al., 2016a, *ApJ*, **819**, L8
- Kelly P. L., et al., 2016b, *ApJ*, **831**, 205
- Kelly P. L., et al., 2018, *Nature Astronomy*, **2**, 334
- Kikuchihara S., et al., 2020, *ApJ*, **893**, 60
- Kim J., Jee M. J., Perlmutter S., Hayden B., Rubin D., Huang X., Aldering G., Ko J., 2019, *ApJ*, **887**, 76
- Klypin A. A., Shandarin S. F., 1983, *MNRAS*, **204**, 891
- Kneib J.-P., Natarajan P., 2011, *A&ARv*, **19**, 47
- Kneib J. P., Mellier Y., Fort B., Mathez G., 1993, *A&A*, **273**, 367
- Kneib J.-P., Ellis R. S., Smail I., Couch W. J., Sharples R. M., 1996, *ApJ*, **471**, 643
- Livermore R. C., Finkelstein S. L., Lotz J. M., 2017, *ApJ*, **835**, 113
- Lotz J. M., et al., 2017, *ApJ*, **837**, 97
- Mahler G., et al., 2018, *MNRAS*, **473**, 663
- Mahler G., et al., 2023, *ApJ*, **945**, 49
- Maizy A., Richard J., de Leo M. A., Pelló R., Kneib J. P., 2010, *A&A*, **509**, A105
- McElwain M. W., et al., 2023, arXiv e-prints, [p. arXiv:2301.01779](https://arxiv.org/abs/2301.01779)
- Medezinski E., Umetsu K., Okabe N., Nonino M., Molnar S., Massey R., Dupke R., Merten J., 2016, *ApJ*, **817**, 24
- Meena A. K., et al., 2023a, *MNRAS*, **521**, 5224
- Meena A. K., et al., 2023b, *ApJ*, **944**, L6
- Meneghetti M., Bartelmann M., Moscardini L., 2003, *MNRAS*, **340**, 105
- Meneghetti M., Bartelmann M., Jenkins A., Frenk C., 2007a, *MNRAS*, **381**, 171
- Meneghetti M., Argazzi R., Pace F., Moscardini L., Dolag K., Bartelmann M., Li G., Oguri M., 2007b, *A&A*, **461**, 25
- Meneghetti M., et al., 2017, *MNRAS*, **472**, 3177
- Merten J., et al., 2011, *MNRAS*, **417**, 333
- Miller T. B., et al., 2018, *Nature*, **556**, 469
- Monna A., et al., 2014, *MNRAS*, **438**, 1417
- Monna A., et al., 2015, *MNRAS*, **447**, 1224
- Mullis C. R., Rosati P., Lamer G., Böhringer H., Schwöpe A., Schuecker P., Fassbender R., 2005, *ApJ*, **623**, L85
- Naidu R. P., et al., 2022, arXiv e-prints, [p. arXiv:2208.02794](https://arxiv.org/abs/2208.02794)
- Nelson E. J., et al., 2023, *ApJ*, **948**, L18
- Nonino M., et al., 2023, *ApJ*, **942**, L29
- Ofek E. O., 2014, MAAT: MATLAB Astronomy and Astrophysics Toolbox, Astrophysics Source Code Library, record ascl:1407.005 ([ascl:1407.005](https://ascl.net/1407.005))
- Oguri M., Takada M., Okabe N., Smith G. P., 2010, *MNRAS*, **405**, 2215
- Oguri M., Bayliss M. B., Dahle H., Sharon K., Gladders M. D., Natarajan P., Hennawi J. F., Koester B. P., 2012, *MNRAS*, **420**, 3213
- Okabe N., Okura Y., Futamase T., 2010, *ApJ*, **713**, 291
- Oke J. B., Gunn J. E., 1983, *ApJ*, **266**, 713
- Owers M. S., Randall S. W., Nulsen P. E. J., Couch W. J., David L. P., Kempner J. C., 2011, *ApJ*, **728**, 27
- Pascale M., et al., 2022, *ApJ*, **938**, L6
- Price-Whelan A. M., et al., 2018, *AJ*, **156**, 123
- Priewe J., Williams L. L. R., Liesenborgs J., Coe D., Rodney S. A., 2017, *MNRAS*, **465**, 1030
- Redlich M., Bartelmann M., Waizmann J. C., Fedeli C., 2012, *A&A*, **547**, A66
- Richard J., et al., 2014, *MNRAS*, **444**, 268
- Richard J., et al., 2021, *A&A*, **646**, A83
- Rieke M. J., Kelly D., Horner S., 2005, Overview of James Webb Space Telescope and NIRCam's Role. SPIE, pp 1–8, [doi:10.1117/12.615554](https://doi.org/10.1117/12.615554)
- Rieke M. J., et al., 2023, *PASP*, **135**, 028001
- Roberts-Borsani G., et al., 2022, arXiv e-prints, [p. arXiv:2210.15639](https://arxiv.org/abs/2210.15639)
- Rodney S. A., et al., 2015, *ApJ*, **811**, 70

- Rodney S. A., Brammer G. B., Pierel J. D. R., Richard J., Toft S., O'Connor K. F., Akhshik M., Whitaker K. E., 2021, *Nature Astronomy*, **5**, 1118
- Sereno M., Jetzer P., Lubini M., 2010, *MNRAS*, **403**, 2077
- Sharon K., Gladders M. D., Rigby J. R., Wuyts E., Koester B. P., Bayliss M. B., Barrientos L. F., 2012, *ApJ*, **746**, 161
- Springel V., et al., 2005, *Nature*, **435**, 629
- Stanford S. A., et al., 2012, *ApJ*, **753**, 164
- Steinhardt C. L., et al., 2020, *ApJS*, **247**, 64
- Strait V., et al., 2020, *ApJ*, **888**, 124
- Strait V., et al., 2021, *ApJ*, **910**, 135
- Torri E., Meneghetti M., Bartelmann M., Moscardini L., Rasia E., Tormen G., 2004, *MNRAS*, **349**, 476
- Treu T., et al., 2015, *ApJ*, **812**, 114
- Treu T., et al., 2022, *ApJ*, **935**, 110
- Tully R. B., Fisher J. R., 1977, *A&A*, **54**, 661
- Vale A., Ostriker J. P., 2004, *Monthly Notices of the Royal Astronomical Society*, **353**, 189
- Virtanen P., et al., 2020, *Nature Methods*, **17**, 261
- Wallington S., Narayan R., 1993, *ApJ*, **403**, 517
- Wang X., et al., 2015, *ApJ*, **811**, 29
- Wang T., et al., 2016, *ApJ*, **828**, 56
- Weaver J. R., et al., 2023, *arXiv e-prints*, p. arXiv:2301.02671
- Welch B., et al., 2022, *Nature*, **603**, 815
- Williams H., et al., 2023, *Science*, **380**, 416
- Zavala J. A., et al., 2023, *ApJ*, **943**, L9
- Zeldovich I. B., Einasto J., Shandarin S. F., 1982, *Nature*, **300**, 407
- Zheng W., et al., 2014, *ApJ*, **795**, 93
- Zitrin A., 2021, *ApJ*, **919**, 54
- Zitrin A., et al., 2009, *MNRAS*, **396**, 1985
- Zitrin A., et al., 2013a, *ApJ*, **762**, L30
- Zitrin A., Menanteau F., Hughes J. P., Coe D., Barrientos L. F., Infante L., Mandelbaum R., 2013b, *ApJ*, **770**, L15
- Zitrin A., et al., 2014, *ApJ*, **793**, L12
- Zitrin A., et al., 2015, *ApJ*, **801**, 44
- de Lapparent V., Geller M. J., Huchra J. P., 1986, *ApJ*, **302**, L1
- van der Walt S., Colbert S. C., Varoquaux G., 2011, *Computing in Science Engineering*, **13**, 22

This paper has been typeset from a $\text{\TeX}/\text{\LaTeX}$ file prepared by the author.